Journal of the Brazilian Society of Mechanical Sciences and Engineering (2020) 42:340
https://doi.org/10.1007/s40430-020-02412-4

TECHNICAL PAPER

Limitations of simplified models to predict soot formation in laminar flames

L. Zimmer[1,2] · **F. Pereira**[1]

Received: 23 October 2019 / Accepted: 13 May 2020 / Published online: 26 May 2020
© The Brazilian Society of Mechanical Sciences and Engineering 2020

Abstract
Soot formation and radiation are important aspects for combustion problems. In this work, numerical simulations of ethylene coflow laminar flames are used to evaluate soot formation and radiation processes under different modeling approximations. Priority was given for models that were capable of producing detailed information with reduced computational requirements. So, the objective of this work is to show and quantify the importance of heat loss by gas and soot radiation and to quantitatively show the impact of different transport models (a detailed and a simplified) in soot predictions. For soot modeling, a semiempirical two-equation model is chosen for predicting soot mass fraction and number density. The model describes particle nucleation, surface growth and oxidation. For flame radiation, the radiant heat losses (gas and soot) are modeled by using the gray-gas approximation with optically thin approximation. For the chemical kinetics, a detailed approach is employed. It is found that gas and soot components of the radiative heat loss are comparable, with the gas radiation being larger (65%). To capture 99.9% of the total heat loss, the numerical domain has to be extended to 2.4 times the flame length based on the stoichiometric mixture fraction. Radiation modeling has a large impact on soot predictions. An error of 19% in the peak soot volume fraction is found when radiation is neglected. Errors due to simplified transport properties are also around 21%.

Keywords Diffusion flame · Soot modeling · Radiation

1 Introduction

Combustion is still the most important energy conversion process in the world. Nevertheless, combustion is responsible for the major part of human emissions of gaseous pollutants and particulate matter to the atmosphere, resulting in negative impacts to the environment and health of humans and animals [1–4]. Thus, many research and development efforts are driven by the increasing need to enhance the efficiency of combustion processes and to reduce pollutant emissions. In order to achieve these goals, a fundamental understanding of the major phenomena of combustion processes is required. In this scenario, modeling tools that are able to predict the main characteristics of flames with low computational cost are of great interest for the industrial and the scientific communities.

Addressing all the phenomena combustion processes can be a major challenge for numerical simulations. For example, the flow turbulence interacts with chemical reactions and thermal radiation, requiring extremely refined meshes to capture the scalar fluctuations or demanding closure models to solve averaged equations. Laminar flames, in which turbulence effects are not present, are a good target to the validation of models, however, even laminar flame calculations can be challenging when detailed properties are taken into account. The present study is concerned with laminar non-premixed flames where soot formation and radiation emission are of interest. Those aspects are clearly found on ethylene diffusion flames, in which a relative high amount of soot is formed and radiative heat loss plays an important role. Focus is given to radiation modeling and transport

Technical Editor: Mario Eduardo Santos Martins, Ph.D.

✉ L. Zimmer
leo.zimmer@mecanica.ufrgs.br

[1] Mechanical Engineering Department, Federal University of Rio Grande do Sul, Rua Sarmento Leite, n. 425, Porto Alegre, Brazil

[2] Department of Mechanical and Industrial Engineering, Ryerson University, 350 Victoria St., Toronto, ON M5B 2K3, Canada

properties evaluation techniques that are capable of producing detailed information on sooting flames with reduced computational requirements.

The importance of radiative heat transfer in sooting diffusion flames has been widely recognized [5–7], but the computational cost is still an important factor for the radiation model selection for multidimensional CFD simulations [8]. The work of Liu et al. [5] presented the overall effect of radiation heat losses on a sooting ethylene diffusion flame. In such work, the authors used a detailed gas-phase reaction mechanism and detailed thermal and transport properties. For the radiation model, they used two approaches, a more complex and computational expensive, based on discrete-ordinates method coupled with a statistical narrow-band correlated-*K* (SNBCK), and a simpler model based on the optically thin model (OTA). The results showed that both gas and solid phases were important to the accurate prediction of flame structure and soot concentrations. Also, the results with the OTA model presented overall good agreement with the results from the more complex radiation model. The work of Demarco et al. [7] explored the overall effect of radiation on a series of diffusion flames. The authors presented the importance of coupling soot and gas radiation properties with some flame key parameters, such differences in peak temperature, peak soot concentration and radiation fraction. Nevertheless, in such works there are only a few qualitative comparisons on radiation components and how they are spatially distributed along the flame. This information is important in order to find which radiative sources are the most important for modeling purposes, and what to expect from the effect of these radiation components along the flame height.

Another important aspect which determines the fidelity of the simulated physical process is the evaluation of multicomponent transport properties in flames, which is also a time-consuming task with a large portion of that time devoted to compute the diffusion fluxes [9–11]. The most accurate approach to compute the diffusion fluxes is solving the multicomponent diffusion equations, derived from the kinetic theory, and can be found on textbooks such as [12–14]. Nevertheless, this approach remains extremely expensive since it relies on the inversion of linear equation systems at each iteration and each computing node [11, 15]. Therefore, the mixture-averaged approach is very popular, since it is a good approximation of the full multicomponent transport equation [11]. It is based on an averaging procedure, and its computational cost is about $\mathcal{O}(N^2)$, with N being the total number of species transported. Another approach to calculate the diffusion coefficients which is frequently used is to consider constant (non-unit) or unitary Lewis Number, which may cost $\mathcal{O}(N)$ [11], but with a general trade-off on the accuracy of the results.

Studies on quantifying the effect of simplified transport models on the flame structure have been published in the literature [9, 15–19]. Nevertheless, those studies were applied to different fuels and flames configurations than the one of interest, such as in: counterflow diffusion flames of H_2–O_2 [16], or CH4/O2–N2–He [17]; a steady, turbulent, nitrogen-diluted hydrogen–air diffusion flame [18]; one-dimensional adiabatic premixed flames [15]; and finally, one-dimensional tubular and counterflow flames, and a coflow flame for a range of fuels [19]. Furthermore, all the above studies neglected soot formation.

In [11], the constant non-unity Lewis number assumption in chemically reacting flows is investigated. In that work, the authors compared detailed transport properties (mixture-averaged approach) against the commonly used unity and non-unity Lewis number approach for calculating diffusivity coefficients. The comparison was done in a range of flames, from 1D laminar to 3D turbulent flames. The mixture-averaged approach is used as reference, and the results suggested that the constant non-unity Lewis number approximation leads to small errors. For the laminar ethylene flame, a pressurized C_2H_4–N_2/air coflow diffusion flame, which is one of the target flames selected for the 2014 and 2016 International Sooting Flame (ISF) Workshops, was assessed. Nevertheless, in such flame no significant soot is presented, so the effect of such Lewis Number assumptions on the production of soot and then its interaction with the flame structure is not found.

The present work explores the effect of considering a simplified approach for calculating transport properties in a sooting laminar flame. Additionally, a detailed evaluation of the radiative components and their spatial distribution is presented.

The radiative heat losses (gas and soot) will be modeled by using the optically thin approximation (OTA). The quantification of each radiation component (from H_2O, CO_2, CO and CH_4 gas-phase species and soot) is then analyzed in detail. For soot modeling, a semiempirical model [5] is chosen since it combines important steps for soot formation, accurate predictability of global soot variables and low computational time, especially for practical combustion systems. Detailed chemical kinetics is used to track the evolution of the gas-phase species responsible for soot nucleation, surface growth and oxidation processes. To compute multi-component transport and thermal properties, detailed and simplified approaches are employed. The effect of such simplifications is evaluated and compared to that of the most detailed solution.

2 Numerical model

For the coflow flame simulations, the conservation equations for total mass, momentum, mass of species and energy are used in cylindrical coordinates along with the respective constitutive relations. This system of equation can be found elsewhere as in [12, 14, 20, 21].

2.1 Soot model

The soot model used in this work is based on [5] with the addition of soot diffusion terms in order to improve the numerical stability. This model is a semiempirical acetylene-based model that describes soot particle nucleation, surface growth and oxidation. It is similar to the model used in a previous work of our group for one-dimensional ethylene flames [22] and only differs in the surface growth rate $k_2 = 1.75 \times 10^3 \exp\left(\frac{-10{,}064}{T}\right)$ and the thermophoretic velocity constant $C_i = 0.65$. Both modifications were proposed in [5] to improve the accuracy for a multi-dimensional configuration. A brief description of the model is given in this section, and the reader is referred to [22] for more details.

Two additional equations are included in the system of conservation equations, one for soot mass fraction, Y_S, and another for soot number density, N_S. The two-dimensional conservation equations for soot mass fraction and soot number density in cylindrical coordinates (r, z) read

$$\begin{aligned}\frac{\partial(\rho Y_S)}{\partial t} &+ \rho u\frac{\partial(Y_S)}{\partial z} + \rho v\frac{\partial(Y_S)}{\partial r}\\ &= -\frac{\partial(\rho V_{T,z} Y_S)}{\partial z} - \frac{1}{r}\frac{\partial(r\rho V_{T,r} Y_S)}{\partial r}\\ &\quad + \frac{\partial}{\partial z}\left(\rho D_s \frac{\partial Y_S}{\partial z}\right) + \frac{1}{r}\frac{\partial}{\partial r}\left(r\rho D_s \frac{\partial Y_S}{\partial r}\right)\\ &\quad + \dot{w}_{Y_S},\end{aligned} \tag{1}$$

$$\begin{aligned}\frac{\partial(\rho N_S)}{\partial t} &+ \rho u\frac{\partial(N_S)}{\partial z} + \rho v\frac{\partial(N_S)}{\partial r}\\ &= -\frac{\partial(\rho V_{T,z} N_S)}{\partial z} - \frac{1}{r}\frac{\partial(r\rho V_{T,r} N_S)}{\partial r}\\ &\quad + \frac{\partial}{\partial z}\left(\rho D_s \frac{\partial N_S}{\partial z}\right) + \frac{1}{r}\frac{\partial}{\partial r}\left(r\rho D_s \frac{\partial N_S}{\partial r}\right)\\ &\quad + \dot{w}_{N_S},\end{aligned} \tag{2}$$

where ρ is the mixture density (kg m^{-3}), u and v are the axial and radial fluid velocities (m s^{-1}), respectively, V_T is the thermophoretic velocity of the soot particles (m s^{-1}), D_s is the soot diffusion coefficient (m^2 s^{-1}), $\dot{w}_{Y_S}$ and $\dot{w}_{N_S}$ are the source terms of soot mass fraction (kg m^{-3} s^{-1}) and soot number density (particles m^{-3} s^{-1}), respectively, and D_s is set to 1×10^{-6} (m^2 s^{-1}), a small value (1%) compared to the average gas diffusivity, in order to overcome numerical instabilities as suggested by [23]. The thermophoretic velocity of soot, V_T, is modeled as

$$V_{T,x_i} = -C_i \frac{\mu}{\rho}\frac{1}{T}\frac{\partial T}{\partial x_i}, \quad (x_i = z, r), \tag{3}$$

where μ is the mixture dynamic viscosity (kg m^{-1} s^{-1}) and T is the temperature (K).

The soot reactions are presented in Table 1. For soot formation, the model employs acetylene (C_2H_2) as the soot precursor species and as the species responsible for surface growth. This is a simplified assumption, since the scientific community recognizes the importance of polycyclic aromatic hydrocarbons (PAHs) in the nucleation, condensation and surface growth processes. The soot oxidation is modeled by the third, fourth and fifth reactions which represent surface oxidation by O_2, OH and O, respectively.

The source terms for soot mass fraction, Eq. (1), and soot number density, Eq. (2), are:

$$\dot{w}_{Y_S} = M_S\left(2R_1 + 2R_2 - R_3 - R_4 - R_5\right), \tag{4}$$

$$\dot{w}_{N_S} = \frac{2}{C_{min}} N_A R_1, \tag{5}$$

where $M_S = 12.011$ (kg kmol^{-1}) is the carbon molar mass, $C_{min} = 700$ is the average number of carbon atoms in the incipient soot particle and $N_A = 6.022 \times 10^{26}$ (particles kmol^{-1}) is Avogadro's number. Equation (4) takes into account soot nucleation, surface growth and oxidation by O_2, OH and O, while Eq. (5) takes into account the production of particles by soot nucleation only. More details about the soot reactions can be found in [22].

It is important to note that this model neglects many phenomena involved in soot formation. Some examples are the central role of PAHs in the soot nucleation and condensation, the reversibility of the elementary steps that lead to nucleation and condensation, the particle size distribution (here it is assumed a monodisperse aerosol), the destruction of particles by coalescence and the formation of large structures by coagulation. Nevertheless, the simplified soot model

Table 1 Soot reactions

Reaction		Rate n.
Nucleation	$C_2H_2 \rightarrow 2C_S + H_2$	R_1
Surf. growth	$C_2H_2 + nC_S \rightarrow (n+2)C_S + H_2$	R_2
Oxid. by O_2	$C_S + \frac{1}{2}O_2 \rightarrow CO$	R_3
Oxid. by OH	$C_S + OH \rightarrow CO + H$	R_4
Oxid. by O	$C_S + O \rightarrow CO$	R_5

parameters can be tailored to reproduce experimental data as in [5] (which inevitably incorporates cancelation of errors from the gas-phase and soot mechanisms, radiation modeling, thermophysical properties and boundary conditions, for example). The present study shows, under some simplified assumptions, the expected effects on soot predictions when frequently used models for transport properties and radiation are chosen. In a more advanced model [24] based on pyrene (a 4-aromatic ring species, A_4) as the soot precursor and taking the particle size distribution into account, it is shown that the changes in C_2H_2 are well correlated with the changes in A_4 when the fuel or oxidant-diluent species changes from N_2 to CO_2, which consequently affects the mass diffusivities of C_2H_2 and A_4. Although not linear, the qualitative trend is the same for both species. The effect of different radiation models is explored in [25], and again the same qualitative trends are observed for C_2H_2 and A_4. The effect of different detailed diffusion models on the soot volume fraction of diffusion flames is presented in [26]. Thus, the present model can be considered a good first approximation for the purposes of the present work, i.e., to evaluate the effect of adiabatic and unity Lewis number approximations in soot predictions for ethylene coflow laminar flames.

The soot volume fraction, f_v, is found from the computed soot mass fraction as

$$f_v = \frac{\rho Y_S}{\rho_C}, \tag{6}$$

where $\rho_C = 1900$ (kg m^{-3}) is the soot density.

2.2 Radiation model

In this work, the optically thin approximation (OTA) is used to model the gas and soot radiative heat losses, similar to [27–30]. With this gray-gas approximation, there is no dependence on the wave number, and the optically thin medium does not scatter nor reabsorbs radiation. The participant gas species are H_2O, CO_2, CO and CH_4. Then, the heat source in the energy conservation equation is:

$$q'''_R = q'''_{R,\text{gas}} + q'''_{R,\text{soot}}, \tag{7}$$

$$q'''_{R,\text{gas}} = -4\sigma\kappa(T^4 - T_\infty^4), \tag{8}$$

$$q'''_{R,\text{soot}} = -Cf_vT^5, \tag{9}$$

where T_∞ is the surrounding temperature, σ is the Stefan–Boltzmann constant (5.669×10^{-8} W m^{-2} K^{-4}) and the constant $C = 3.337 \times 10^{-4}$ (W m^{-3} K^{-5}) is taken from [5]. $\kappa = \sum p_{i,\text{atm}}\kappa_i$ denotes the Planck mean absorption coefficient of the mixture (m^{-1}), and $p_{i,\text{atm}}$ and κ_i are, respectively, the partial pressure (atm) and Planck mean absorption coefficient of species i (atm^{-1} m^{-1}). The Plank mean absorption coefficient for H_2O and CO_2 is given in [31] and for CO and CH_4 is given in [32]. Note that in Eq. (9) the effect of the surrounding temperature was neglected since soot is found only at flame regions with high temperatures.

According to [33], the use of OTA radiation model on the target flame (non-smoking flame) resulted in a slight underprediction of the peak centerline flame temperature, when compared to discrete-ordinates method (DOM) with a statistical narrow-band correlated-k (SNBCK) model for the absorption coefficients. However, for the purposes of the present work, this slight underprediction of the peak centerline flame temperature does not affect the conclusions presented here. As will be seen later, most of the radiative heat losses are located close to the stoichiometric mixture fraction isosurface, where soot and participating species are found at high temperatures, which are reasonably well captured for the current model.

2.3 Transport properties

In this study, the transport properties are calculated using two different approaches; one is here defined as detailed transport approach, which is more computational demanding, and the other is here defined as simplified transport approach, which has less computational effort.

The detailed approach uses the mixture-average concept to calculate the viscosity μ using the Wilke [34] formula and the thermal conductivity λ using Mason [35] formula. Both expressions can be evaluated at computational cost of about $\mathcal{O}(N)$ [11]. And the diffusion coefficients D_{im} are obtained by employing the Hirschfelder and Curtiss approximation [36], with a computational cost of about $\mathcal{O}(N^2)$.

The simplified approach uses the simplified formulations proposed in [37] for viscosity $\mu/c_p = 1.67 \times 10^{-8}(T/298)^{0.51}$ (kg m^{-1} s^{-1}) and thermal conductivity $\lambda/c_p = 2.58 \times 10^{-5}(T/298)^{0.69}$ (W m^{-1} K^{-1}), while to evaluate the diffusion coefficients for the gas species unitary Lewis Number is assumed ($\text{Le}_i = \lambda/\rho c_p D_i^M = 1$). All the simplified expressions can be evaluated at computational cost of about $\mathcal{O}(N)$.

It is important to highlight that the final computational cost is dependent not only on the selected transport properties approach, but also on the number of computational grid, total number of species, the radiation model and the transport equation solver. The above-mentioned cost is just to guide the model selection and the expected computational time. In the present work, the focus is given to the overall accuracy of both approaches to a specific soot flame, since the overall computational time can be found elsewhere [9, 11].

3 Description of the problem

The target flame in this work is the atmospheric pressure, non-smoking ethylene/air coflow diffusion flame of Santoro et al. [38]. There are significant experimental data available for this flame, and they have been widely studied by many researchers in experimental (e.g., [38–42]) and numerical works (e.g., [33, 43–47]). This flame is also recommended as one of the soot study cases by *International Sooting Flame (ISF) Workshop* [48].

According to the description of [38] and as represented in Fig. 1, the burner consists of two concentric tubes of internal diameters of 11.1 mm and 101.6 mm, with the fuel flowing through the central tube and air through the outer passage. Also, the fuel tube extends 4 mm beyond the exit plane of the air tube. The mean velocity of the fuel stream is 3.98 cm s^{-1} (flow rate 3.85 cm^3 s^{-1}) and of the air stream is 8.9 cm s^{-1} (flow rate 713.3 cm^3 s^{-1}).

4 Numerical method

Figure 1 shows the laminar diffusion coflow and the axisymmetric cylindrical coordinate system. The computational domain is covered in z direction from 0 to 15 cm (with $z = 0$ at the exit plane of the fuel tube) and in the r direction from 0 to 4.75 cm. The mesh is refined in the flame region with maximum resolution of dr = 0.1 mm and dz = 0.2 mm between r = 0.0 cm to 0.555 cm and z = 0.0 cm to 10.0 cm. A growth ratio of 1.1 is used in the remain of the domain, so that a non-uniform mesh is created to save computational time while solving large spatial gradients. It was found that further refinement did not change the variables analyzed in the present work. Therefore, the total number of volumes for the current domain was 47,241. The fuel stream is pure ethylene, and the oxidizer stream has the simplified composition of standard dry air (Y_{O_2} = 0.233 and Y_{N_2} = 0.767). Fully developed flow velocity profile was assumed for the fuel stream, and a boundary-layer-type velocity profile was assumed for the air stream at their respective inlet surfaces. The inlet temperature is set to 300 K for both streams. In order to isolate the preheating effects of the fuel tube and fuel stream from our analysis, no extension of the fuel tube is accounted for and the tube wall thickness (r = 0.555 cm) is set to zero. The importance of these boundary conditions was studied somewhere else [45, 49, 50] and will not be the focus of the present study. The wall was treated as a free-slip wall condition and the exit of the domain was treated as an outflow boundary condition.

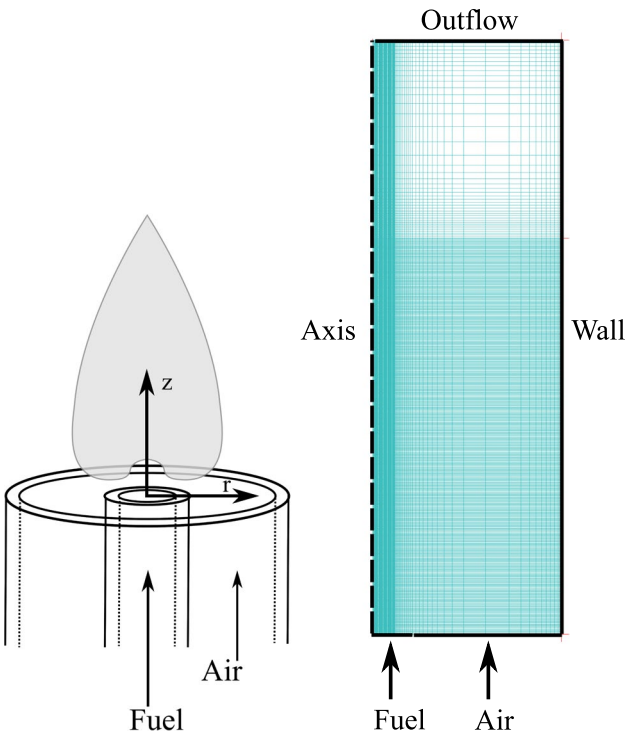

Fig. 1 Laminar diffusion coflow representation: axisymmetric coordinate system (left); axisymmetric numerical domain with an example of mesh distribution (right)

The system of equations for axisymmetric coordinate system was solved with the commercial CFD software ANSYS FLUENT v.16.1 [51] for steady-state conditions. It used a segregated pressure-based solver with the SIMPLE algorithm to treat the pressure and velocity coupling. The advective terms were discretized by second-order upwind, while the diffusion terms were discretized by second-order central differencing.

The soot equations [Eqs. (1) and (2)] are introduced through a user-defined function (UDF) and are solved for each iteration along with the remaining conservation equations. The results of the soot model are taken into account by treating soot as a new gas species. Also additional source terms for species related to soot formation and oxidation (C_2H_2, H_2, CO, H, O_2, OH and O) are added to the system of equations. Thus, the elements are conserved, and the summation of species mass fractions is equal to one ($\sum_{i=1}^{N} Y_i = 1$) and the summation of species source terms (in mass basis) is equal to zero ($\sum_{i=1}^{N} \dot{w}_i = 0$). The mixture density is calculated based on the density of the gas phase only and is calculated by the ideal-gas equation of state using the low-Mach-number approximation. In this way, the interaction between the soot chemistry and the gas-phase chemistry was fully accounted for in the transport equations for the total mass, for the mass of species and for energy. The transport and thermodynamic properties from soot are modeled as the ones from a solid carbon (graphite). The soot advective term was discretized by second-order upwind, and the diffusion terms, including the additional thermophoretic

term, were also discretized by second-order central differencing. The additional thermophoretic diffusion term was lumped into the source term.

The numerical results are sensitive to the choice of kinetic mechanism. A study with different mechanisms is given in "Appendix 1." Nonetheless, the current work follows the choice of the reference work [5], employing a modified version of the kinetic mechanism GRI3.0 [52], without all NO*x*-related reactions. With this mechanism, a total of 37 (36 gas + graphite) species and 219 reactions were considered. Thermodynamic and transport properties were taken from kinetic mechanism GRI3.0. The simplified approach for transport properties as well as the OTA radiation model was also included in the system of equation through UDFs.

5 Results

Although not being the aim of the present work, it is instructive to compare the model results with experimental data in order to quantify the model prediction capability. No attempt was made to adjust the soot model parameters to achieve a better agreement. So, in the first part a comparison of the current model against experimental results is presented. In the second part, the structure of the simulated ethylene coflow flame is discussed in detail as well as the importance of each component in the heat loss due to radiation. In the last part, the effect of the choice of transport properties and radiation on the model predictions is explored.

5.1 Comparison with experimental data

Figure 2 shows the comparison between experimental data from [39] and the present simulation for the axial velocity as function of the radius for four heights above the burner exit face.

It is possible to see that the present simulation has a good agreement with the axial velocity measurements. A small deviation can be seen at the lower height ($z = 10$ mm) near the tube exit ($r = 0$). This deviation can be attributed to the tube and fuel preheating effect (not considered in this simulation), which can modify the inlet velocity profiles. It is possible to see that the axial velocity increases with the high above the burner. This is due to the gas expansion and buoyancy effects as will be shown later.

The predicted radial temperatures at four heights above the burner exit are shown in Fig. 3. The comparison with the experimental data shows good agreement at the outer region of the flame, but could not correctly predict the measured temperatures near the tube centerline; for example, at the height of 10 mm, the absolute (and relative) difference is 380 K (33%) and at 70 mm is 120 K (7%). This discrepancy can be attributed to the choice of kinetic mechanism as well as the preheating effect of the fuel tube and fuel stream, which was neglected in this work. Some simulations [45, 49, 50] of ethylene coflow flames, with similar configurations to this target flame, analyzed the influence of wall boundary condition of fuel tube on the flame. In [49], a temperature profile for the fuel tube is assumed, in [50], isothermal and adiabatic wall treatments are evaluated, and in [45], conjugate heat transfer (CHT), isothermal and adiabatic wall treatments were compared. The main result of all these works is that the flame preheating effect has a significant influence on the prediction of flame temperature and species, including soot, especially on the centerline. According to [45], when CHT is used, the soot formation predictions on the centerline is improved, since the model is able to capture the fuel pyrolysis that occurs inside the fuel tube. Results from [49], showed that the velocity profiles of both streams at the nozzle exit are neither fully developed nor uniform profiles. Therefore, from the result presented above it is expected some discrepancies in temperature, in gas-phase species and therefore in the amount of soot predicted by the current simulation.

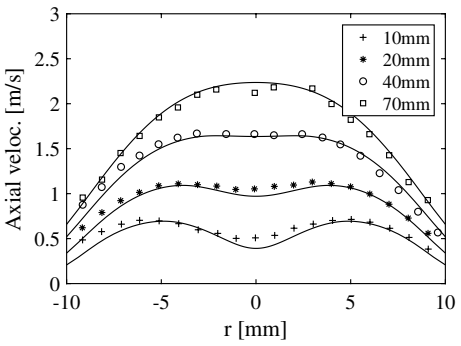

Fig. 2 Axial velocity comparison for four heights; symbols: experimental data [39]; solid line: present simulation

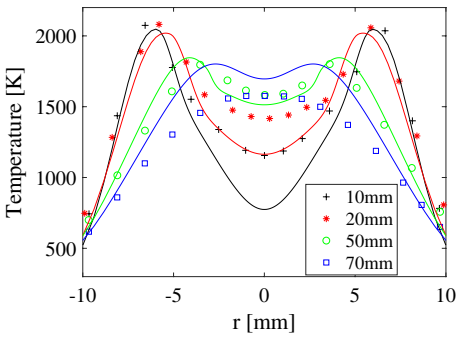

Fig. 3 Temperature comparison; symbols: experimental data [39]; color solid lines: present simulation. (For interpretation of the references to color in this figure, the reader is referred to the online version of this article.)

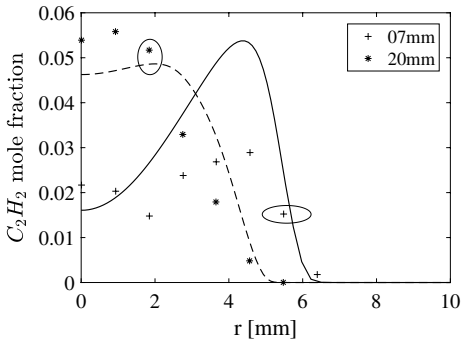

Fig. 4 Radial C_2H_2 mole fraction comparison; symbols: experimental data [40]; solid lines: present simulation

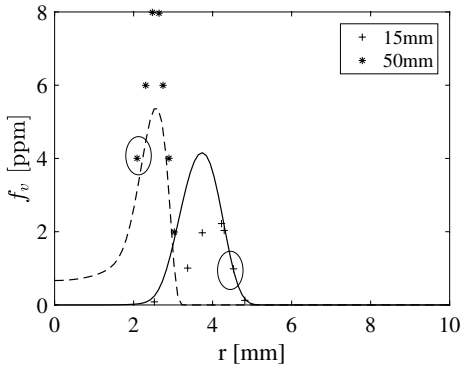

Fig. 5 Radial f_v comparison; symbols: experimental data [39]; lines: present simulation

Figure 4 shows the comparison for C_2H_2 mole fraction radial profile at two heights. The correct prediction of acetylene field is important in the current modeling since the nucleation (R1) and surface growth (R2) are directly dependent on it. The model can provide a good qualitative approximation for the distribution of C_2H_2 mole fraction, but not the exact values. For example, close to the fuel tube ($r = 5.55$ mm and $h = 7$ mm) the model overpredicts the acetylene concentration in 1.85 times; $X_{C_2H_2,sim} = 0.054$ instead of $X_{C_2H_2,exp} = 0.029$. Since this particular region is extremely important to soot formation (in this region the first particles are nucleated and start to grow), the prediction of soot formation will be directly affected and important deviations are expected.

The soot amount predicted by the present model is compared to experimental data in two ways. First, the radial profiles of soot volume fraction at two heights above the burner are compared in Fig. 5, which shows that the model can qualitatively predict the soot formation in the radial direction, with values of the same order as the experimental data. While the model overpredicts the soot production at $h = 15$ mm, it underpredicts the soot production at $h = 50$ mm.

The second comparison is done in terms of an integrated soot volume fraction, F_v, defined as:

$$F_v = 2\pi \int_{r=0}^{\infty} r\, f_v(r,h)\, \mathrm{d}r, \tag{10}$$

where h is the height above the fuel tube exit. The comparison of F_v along the height of the flame is presented in Fig. 6 (left). The figure shows that the amount of soot predicted by the model follows the same pattern of formation and oxidation as both experimental works of [39, 41]. The simulated soot formation reached the same maximum integrated value, but in a lower position (29 mm instead of 40 mm). The soot is being formed and oxidized earlier for the present model because the entire flame is shorter, as can be inferred from the comparison of temperature results in Fig. 3. Two approaches can be used to estimate the flame length; the first is based on the decay of F_v, which is $h_{F_v} \approx 70$ mm, and the second approach is the location at the centerline of the flame where the stoichiometric mixture fraction is found, which is $h_{Z_{st}} = 77$ mm. Similar to the previous analysis, both flame length calculations are lower than the experimental value of 88 mm [39]. Figure 6 (right) also presents the normalized F_v as a function of the normalized axial distance (normalization by the flame length based on the location of peak F_v). It is possible to observe that the present soot model gives a

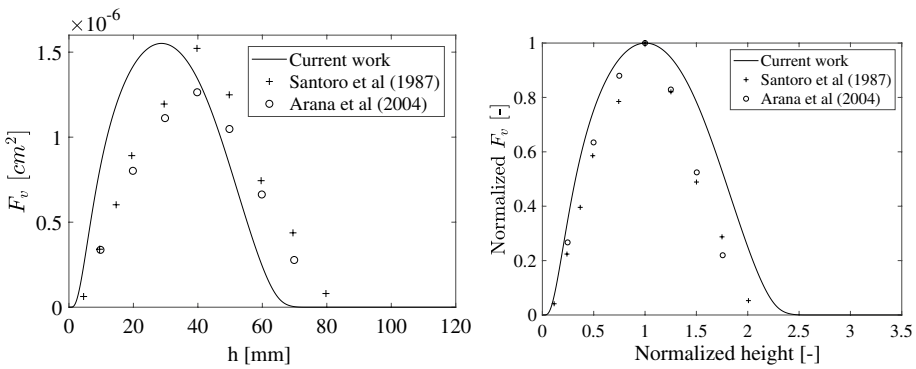

Fig. 6 Left: F_v comparison along the height h of the burner; right: comparison of normalized F_v along normalized height (based on location of peak F_v); symbols: experimental data [39, 41]; solid line: present simulation

reasonable prediction of the integrated soot volume fraction at the formation region. From the top of the flame upward, however, the model clearly underpredicts the soot oxidation rate delaying the decay of F_v.

From this section, it is possible to draw some partial conclusions. The model is able to capture the overall flame characteristics and soot formation. The soot formation is sensitive to the preheating of fuel tube and fuel stream and the choice of kinetic mechanism (comparison shown in "Appendix 1"). It is possible as well to note that there are some intrinsic limitations of the chosen soot model (semiempirical) and the parameters of the soot reactions. An example of the influence of the soot parameters is given in "Appendix 2." Despite all these uncertainties, this model and its results are good enough for the purposes of the present work, i.e., to evaluate the effect of adiabatic and unity Lewis number approximations in soot predictions for ethylene coflow laminar flames.

5.2 Flame structure and radiation analysis

Figure 7 shows two-dimensional details of the flame structure, including temperature, soot volume fraction field, stoichiometric mixture fraction (Z_{st}) isosurface and some flow streamlines. To help the analysis, the fuel tube is schematically drawn at $r = 0.555$ cm. It is interesting to see the effect of the heat loss by gas and soot radiation in the temperature

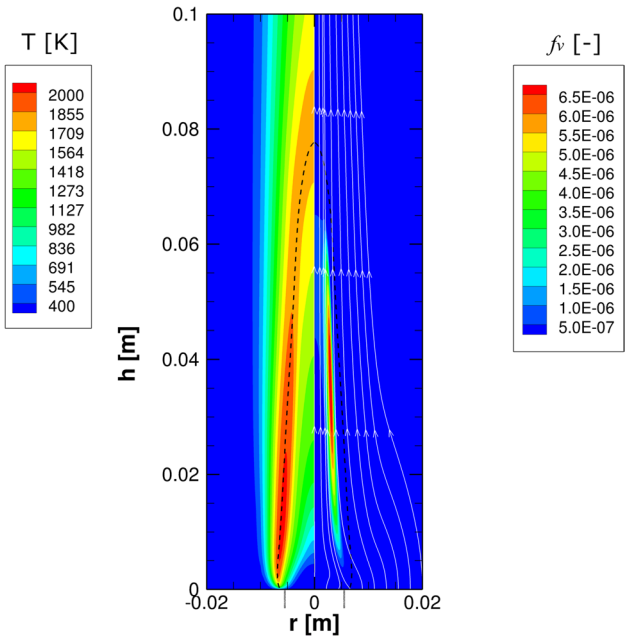

Fig. 7 Flame structure. Left: temperature [K] contour; right: f_v [−] contour with velocity streamlines (solid white lines with arrows); dashed line: $Z_{st} = 0.0637$; fuel tube is drawn at $r = 0.555$ cm; figure in scale (1:1). (For interpretation of the references to color in this figure, the reader is referred to the online version of this article.)

field (left part of Fig. 7), especially downstream, making the high-temperature region limited in a small "wing" area. This area lies around the stoichiometric Z_{st} line, and the maximum temperature predicted was 2050 K. In the right part of the figure, the f_v field is presented. The soot field is restricted to a narrow area located in the fuel-rich zone (within the Z_{st} envelope). The maximum soot volume fraction predicted by the present simulation is $f_{v,max} = 7.1$ ppm, while the experiment of [38] reported $f_{v,\,max} = 9$ ppm, which fits within the uncertainty of experimental measurements of 30%. From the streamlines, we see that the maximum soot volume fraction is found in a streamline which starts at the coflow side, crosses the Z_{st} line toward the fuel-rich zone and leaves the Z_{st} envelope close to the flame tip. Similar description was presented by [39]. The f_v field essentially follows the flow field and is slightly pushed toward the center of the flame by the thermophoretic diffusion. Thus, the soot nucleates in the fuel-rich side of the flame, close to the flame base, and grows up to a flame height of 30 mm. From this point upward, f_v starts to decrease due to surface oxidation and at $h = 60$ mm it is almost completely consumed.

Figure 8 shows in detail the field of acetylene (C_2H_2) mass fraction and the distributions of the soot production/consumption reactions along the flame. It is possible to notice some aspects of the soot formation process. First, looking at the distribution of the peak of the reactions, the ones responsible for soot formation are spatially wider at the base of the flame than the reactions of oxidation at the top of the flame. Second, the intensity of the reactions is different. For example, the nucleation rate is about 1000 times lower than the surface growth rate, and the oxidation by OH is about 10 times higher than the surface growth rate. Thus, for the present flame, soot formation is dominated by surface growth reaction, and soot consumption is dominated by the oxidation by OH. Third, the nucleation of the first particles starts at the fuel side of the flame, but at a radial distance beyond the tube ($r > 0.555$ cm). Note that for a laminar diffusion flame, the flame shape quickly adapts to the fuel flow rate and, in the present case, the flame diameter at the base of the flame is larger than the tube diameter. Thus, nucleation takes place in the fuel-rich region of the flame, close to the temperature peak and to the highest concentrations of C_2H_2. Lastly, not only the soot field is within the Z_{st} envelope, but all its source term distributions.

The flame is also affected by the heat loss due to the gas and soot radiation, which is shown in Fig. 9. The figure shows the comparison of the temperature profile with the main components of heat loss by radiation. It is possible to see that the peak radiative heat loss rate of the soot is one order of magnitude higher than that of the gas, but it is confined to a narrow area. From all gas-phase species which participate in the gas radiation (H_2O, CO_2, CO and CH_4), the CO_2 contribution is dominant, as shown on the left of

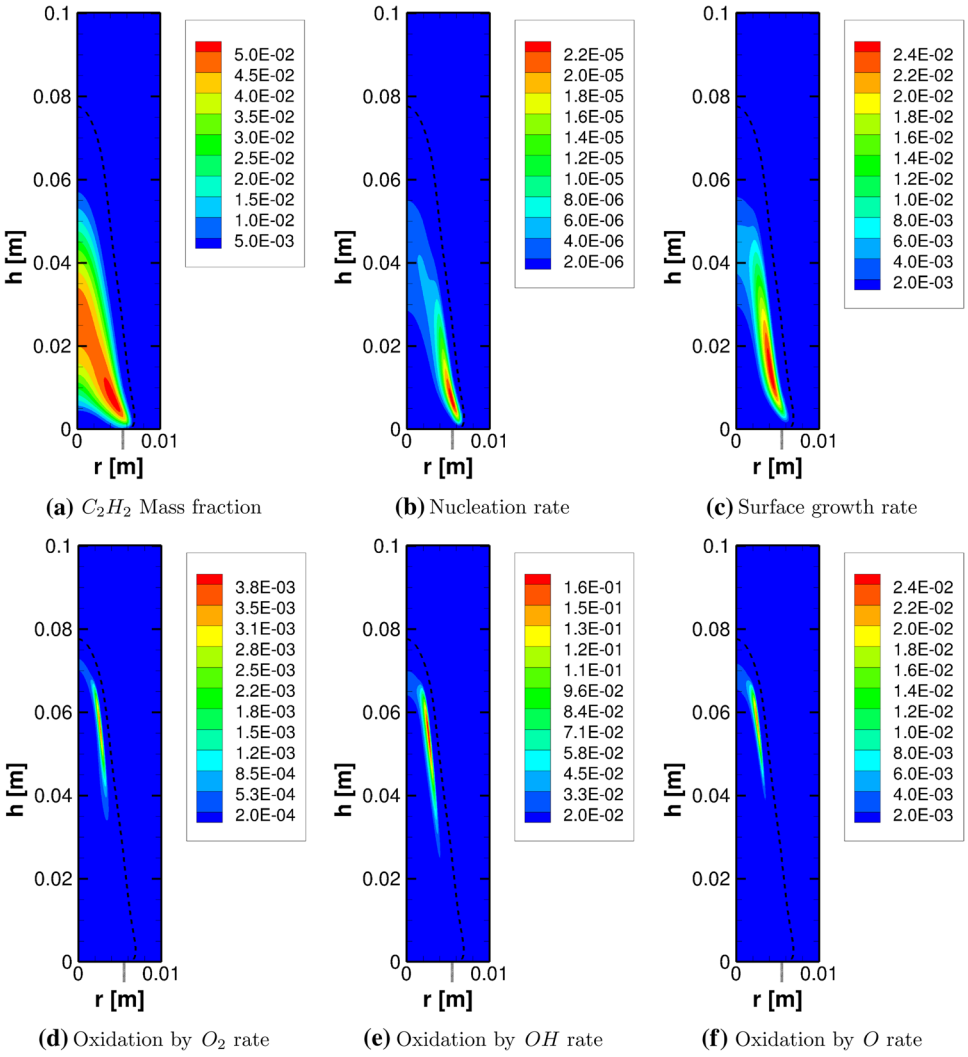

(a) C_2H_2 Mass fraction **(b)** Nucleation rate **(c)** Surface growth rate

(d) Oxidation by O_2 rate **(e)** Oxidation by OH rate **(f)** Oxidation by O rate

Fig. 8 C_2H_2 Mass fraction [−] and reaction rates [kmol/m^3 s]; dashed line: $Z_{st} = 0.0637$; fuel tube is drawn at $r = 0.555$ cm; figures are not in scale. (For interpretation of the references to color in this figure, the reader is referred to the online version of this article.)

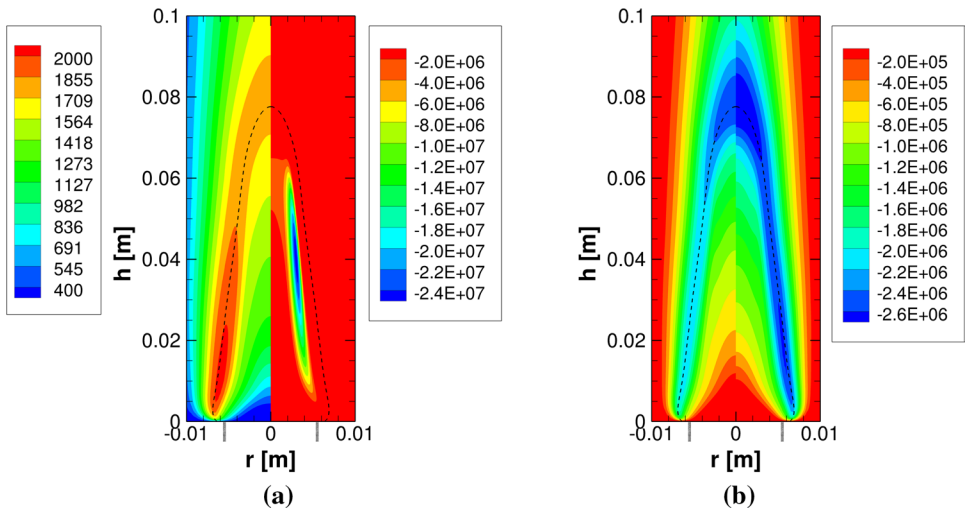

(a) **(b)**

Fig. 9 Comparison of temperature and radiation components; **a** left: temperature [K] contour; right: soot radiation source term [W/m^3]; **b** left: CO_2 radiation component in the source term [W/m^3]; right: total gas source term [W/m^3]; dashed line: $Z_{st} = 0.0637$; fuel tube is drawn at $r = 0.555$ cm; figures are not in scale. (For interpretation of the references to color in this figure, the reader is referred to the online version of this article.)

Fig. 9b. Also the soot radiation source term is located in the inner part of the flame (within the Z_{st} envelope), while the total gas-phase radiative source term is located in a broader region of the flame along the Z_{st} line.

In this work, the gas and soot radiative heat losses were also assessed by computing the respective cross-sectional integrated radiative source term as

$$Q_{R,i} = 2\pi \int_{r=0}^{\infty} r\, q_i'''(r,h)\, \mathrm{d}r, \tag{11}$$

where the radiative source terms q_i''' are taken from Eqs. (7), (8) and (9), for total, gas and soot contributions, respectively. The contribution of each component to the total radiation along the height above the burner is shown in Fig. 10.

Figure 10 shows that both phases have an equivalent importance for the most part of the flame length (around 70 mm). The soot contribution is more intense than the gas only in the small region where soot is found in higher quantities. In the region where soot reaches the maximum formation, its radiation emission contributes up to 60% for the total radiation in that height above the burner. The gas radiation plays an important role throughout the whole flame and is dominant at the flame base and for the post-flame region. The total contribution of each phase was calculated integrating the previous results along the height. It was found that the gas-phase radiation is the most important contribution, being responsible for 62% of the total radiative heat loss. Thus, even though confined to a small area, soot radiation also plays an important role, being responsible for the remaining 38%.

5.2.1 Cumulative radiation effect along the flame height

In order to investigate the effect of the gas-phase radiation in the post-flame region, additional simulations were done extending the domain in axial direction. Figure 11 shows the cross-sectional integrated radiative source term and its cumulative value along the height above the burner.

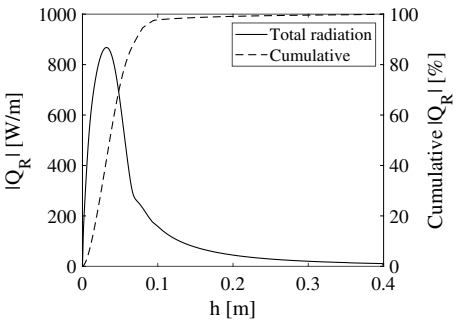

Fig. 11 Integrated radiation source term along the height and cumulative value

The total radiation decays exponentially in the post-flame region, as shown in Fig. 11, and at $h = 0.4$ m, the total radiation is about 1% of maximum of Q_R (found at $h = 0.0315$ m). With the increase in the computational domain, the gas-phase radiation increases to 65%, of the total heat loss, and consequently, the soot radiation decreases to 35%. To calculate the relative cumulative value, an extrapolation was done in order to find the maximum cumulative value. With that extrapolation, one could also estimate the height where $Q_R \approx 0$, which is $h \approx 1.92$ m. This relative cumulative radiation along the height can be used as a guide to determine the length of the numerical domain. Table 2 shows the height above the burner in terms of some cumulative Q_R values.

From the table, it is possible to see some interesting results. First, at one flame length ($h = h_{Z_{st}}$) the total radiative emission is about 93%; second, if it is desired to compute over 99% of the radiative effect on the flame, it is necessary at least 2.4 times the flame length; and last, for the simulation with domain ending at $h = 0.4$ m the cumulative radiation effect is more than 99.9%. The table provides a good guideline on determining the length of the numerical domain in order to capture the effect of the radiation heat transfer.

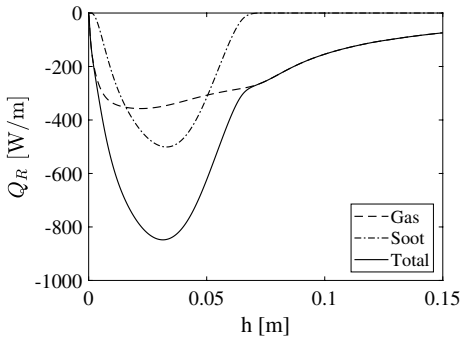

Fig. 10 Integrated radiation source term along the height for the each phase and the combined case

Table 2 Height above the burner corresponding to some cumulative Q_R values

Cumulative Q_R [%]	h [m]	$h/h_{Z_{st}}$
80	0.06	0.74
90	0.07	0.92
93	0.077	1.00
95	0.08	1.07
99	0.19	2.40
99.5	0.27	3.48
99.9	0.39	5.03
100	1.92	24.99

5.3 Radiation and transport properties effects

In this section, the effect of transport properties, explained in Sect. 2.3, is analyzed, in which the simplified approach is evaluated and compared to the more detailed solution. Also the effect of heat loss by radiation is evaluated.

The comparison of temperature fields for the following cases, adiabatic with detailed transport, non-adiabatic with detailed transport, adiabatic with simplified transport, and non-adiabatic with simplified transport, is shown in Fig. 12.

The temperature contours and the Z_{st} line for the same heat loss condition are very similar. The combination of both solid- and gas-phase radiation alters significantly the temperature profile, making the peak temperature to appear at the "wings" of the flame for the non-adiabatic cases (Fig. 12b and d), instead of the centerline when no heat loss is accounted for (adiabatic cases, Fig. 12a and c). Based on the length of Z_{st}, it appears that the flame length of non-adiabatic cases is higher than that of the adiabatic cases. The maximum temperatures found are 2253, 2050, 2301 and 2065 K, for the four cases presented in Fig. 12, respectively. The relative difference between the simplified and the detailed transport approaches within the same heat loss condition $((\phi_{\text{simplified,max}} - \phi_{\text{detailed,max}})/\phi_{\text{detailed,max}})$ is 2.09% and 0.73%, for adiabatic condition and non-adiabatic condition, respectively. Thus, it can be anticipated that the approximate 200K temperature difference between adiabatic and non-adiabatic cases probably has an important impact on species fields and, consequently, on soot production and destruction. On the other hand, the possible effects on species and soot formation due to transport models are not clear. Therefore, the comparison of f_v fields for same cases is presented in Fig. 13.

The similarity of the f_v contours for the same heat loss condition is also found, but differently from the temperature profiles the maximum values of f_v are more influenced by the transport properties choice. The $f_{v,max}$ found are 8.41, 7.09, 6.68 and 5.63 ppm, for the four cases shown, respectively. The relative difference in terms of $f_{v,max}$ between the simplified and the detailed transport approaches within the same heat loss condition is exactly same, − 20.6%, for adiabatic condition and non-adiabatic conditions. The difference between adiabatic and non-adiabatic cases for both transport approaches is same, 18.7%. In addition to the f_v field comparison, a new assessment of the integrated soot volume fraction F_v for the four cases is done and shown in Fig. 14.

It is possible to see some additional aspects. First, the soot formation and destruction rates, and therefore the soot amount, for the same heat loss conditions are similar. Second, the flame length, based on the decay of F_v, for the adiabatic cases is shorter than for the non-adiabatic cases. Similar conclusion was drawn before from analyzing the extent of Z_{st} in the centerline.

It is clear that the radiation has a first-order effect on predicting the flame characteristics and soot concentration. The choice of transport properties plays a secondary, but still important, effect on predicting the soot field. Therefore, one could use the simplified approach to gain computational speed while still capturing the basic features of soot formation.

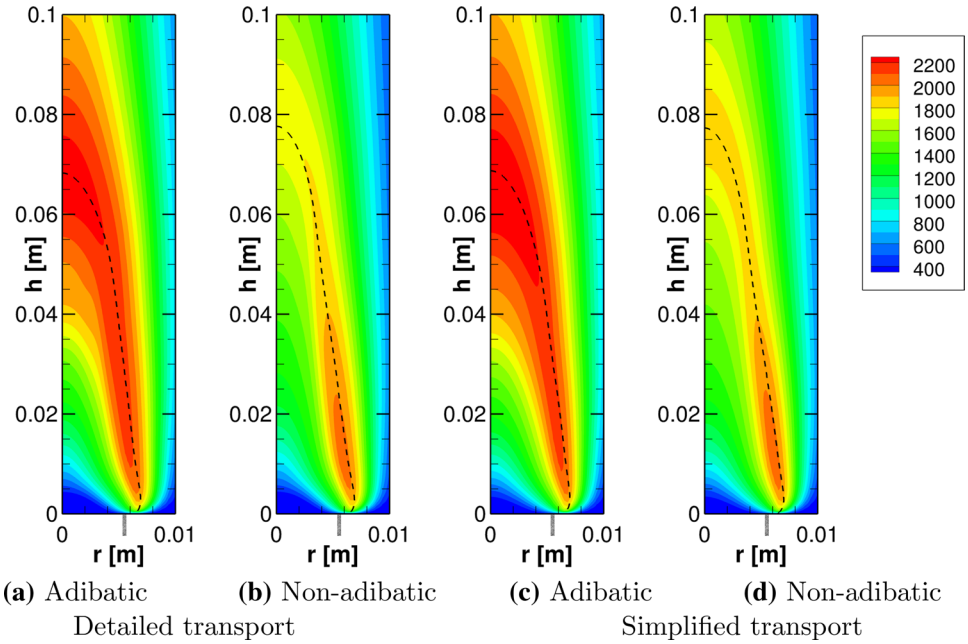

Fig. 12 Radiation and transport properties comparison on the temperature field [K]; dashed line: $Z_{st} = 0.0637$; fuel tube is drawn at $r = 0.555$ cm; figures are not in scale. (For interpretation of the references to color in this figure, the reader is referred to the online version of this article.)

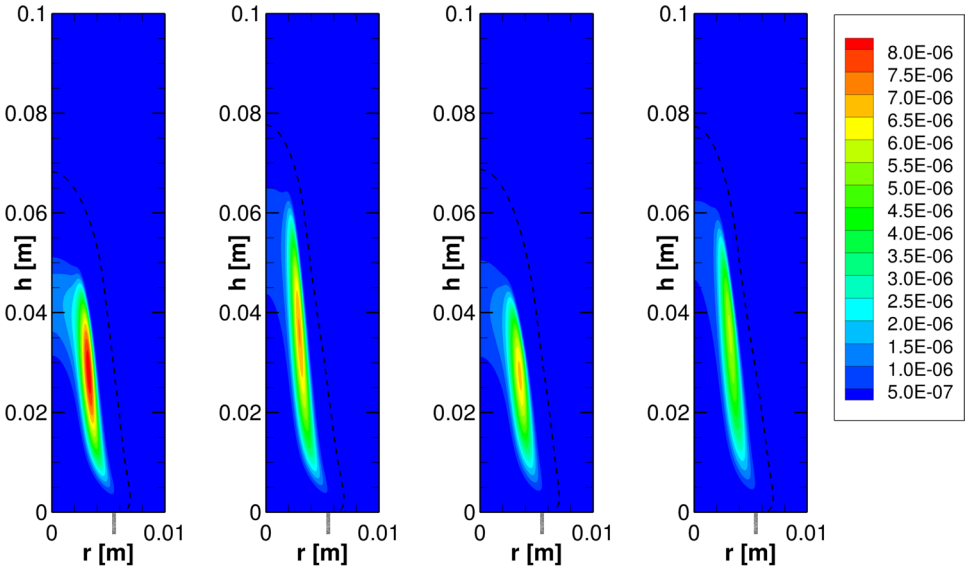

Fig. 13 Radiation and transport properties comparison on the f_v field [−]; dashed line: $Z_{st} = 0.0637$; fuel tube is drawn at $r = 0.555$ cm; figures are not in scale. (For interpretation of the references to color in this figure, the reader is referred to the online version of this article.)

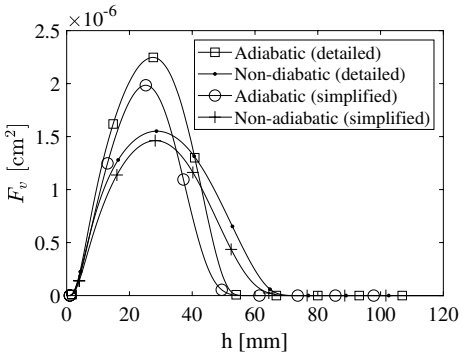

Fig. 14 Heat loss and transport properties comparison on the F_v

6 Conclusions

In this study, soot formation on atmospheric ethylene coflow flame was numerically analyzed. A semiempirical two-equation model was chosen for predicting soot mass fraction and number density. The model describes particle nucleation, surface growth and oxidation. For the gas phase, a detailed kinetic mechanism was considered. The model was implemented in a commercial CFD and assessed against experimental data from the literature. No attempt to modify the soot model was done to achieve better quantitative agreement. The flame structure and the quantification of heat loss by gas and soot radiation were presented in detail. Additionally, the effect of choosing different transport models (detailed or simplified) and considering (or not) the radiation heat loss was discussed.

The target flame in this work was the atmospheric pressure, non-smoking ethylene–air coflow diffusion flame of Santoro et al. [38]. The comparison with experimental data showed that the model could predict the behavior of soot formation, with values of the same order as the experimental data, but with a shorter flame length compared to the experimental value. It was also found that some aspects in numerical modeling can have an important impact on soot predictions and can bring uncertainties to soot modeling, such as the preheating of the fuel tube and the fuel stream, the choice of the kinetic mechanism and the intrinsic limitations of the chosen soot model (semiempirical) and the parameters of the soot reactions.

The flame structure was shown in detail, revealing the relative position to the soot formation area and the stoichiometric mixture fraction envelope. The radiative heat loss rate of the soot is one order of magnitude higher than that of the gas, but it is confined to a narrow area. From all gas-phase species which participate in the gas radiation, the CO_2 contribution is dominant. It was found that the gas-phase radiation is the most important contribution for the entire flame, being responsible for 65% of the total heat loss. Soot was responsible for the remaining 35%. For coupling 99.9% of the radiative heat loss, it was necessary to extend the numerical domain, reaching 2.4 times the flame length based on the stoichiometric mixture fraction position at the centerline.

Additionally, it was found that the gas and soot radiation terms are of primary importance for flame simulations. As a first approximation, the target flame can be simulated using a simplified transport model, with expected errors

in soot volume fraction around 21%. If a more accurate solution is needed, the solution can be resumed with the detailed transport properties.

Acknowledgements The first author acknowledges the financial support of the Coordenação de Aperfeiçoamento de Pessoal de Nível Superior (CAPES) [Project No. BEX5381-13-4].

Compliance with ethical standards

Conflict of interest No potential conflict of interest was reported by the authors.

Appendix 1: Kinetic mechanism influence in soot modeling—1D flames

For the target flame, a variety of kinetic mechanisms have been used for predicting the gas-phase species. A comparison of kinetic mechanisms and its influence in soot prediction is done for 1D counterflow flames. Seven kinetic mechanisms were tested and are presented in Table 3. Simulations were done for ethylene counterflow flames at a stretch rate a of 20 1/s and 100 1/s, for coupled and adiabatic case, using the soot model of [22]. Only the 20 1/s are shown here since the 100 1/s have the same behavior of the 20 1/s. The values for the GRI3.0 reduced

Table 3 Kinetic mechanisms

Mechanism	Size (sp/reac)	Obs.
ABF [53]	101/544	Developed for ethane, ethylene, and acetylene
Blanquart [54]	148/928	Hydrocarbon fuels from methane to iso-octane
GRI Mech v3 [52] (gri3.0)	53/325	Developed natural gas combustion
GRI Mech v3 reduced	36/219	Removed all NOx formation
USC Mech VII [55] (USC II)	111/784	H2/CO/C1–C4 compounds
Wang and Laskin (WL) [56]	75/529	Ethylene and acetylene combustion
Skeletal of WL (sk/WL) [57]	32/206	Skeletal based from Wang and Laskin Mech

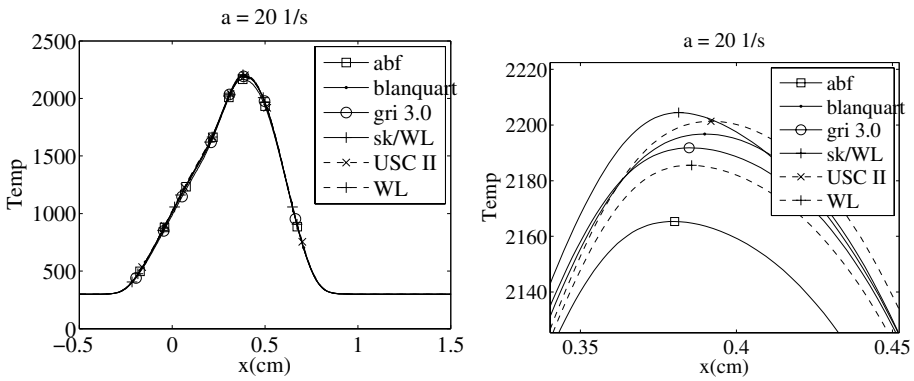

Fig. 15 Temperature profile; zoom at the peak

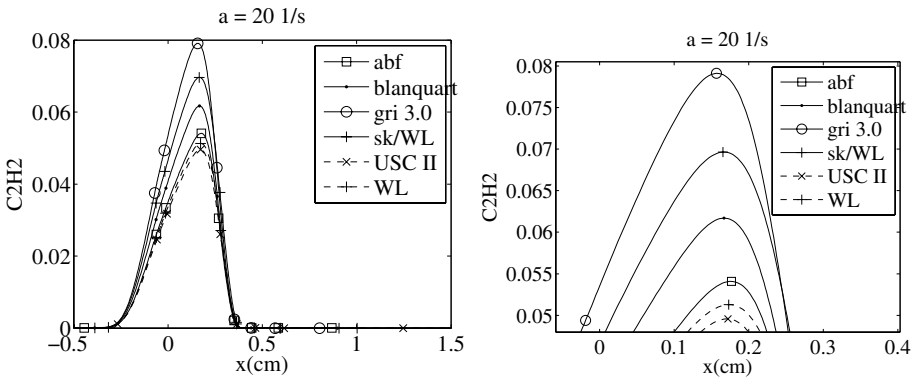

Fig. 16 C_2H_2 mass fraction profile; zoom at the peak

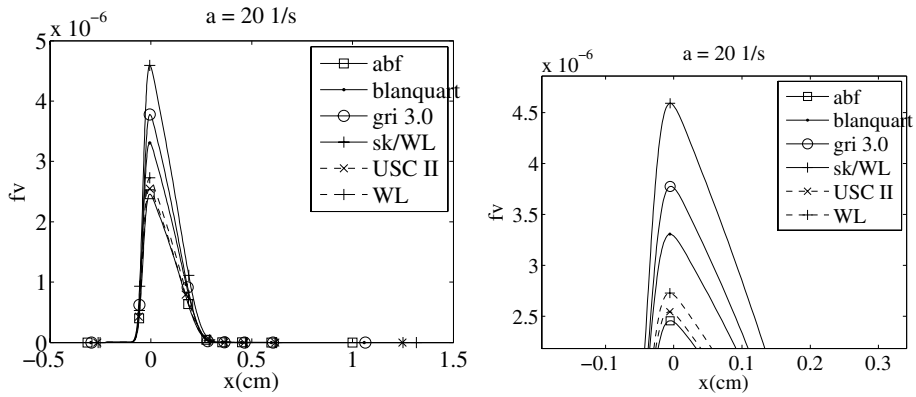

Fig. 17 f_v profile; zoom at the peak

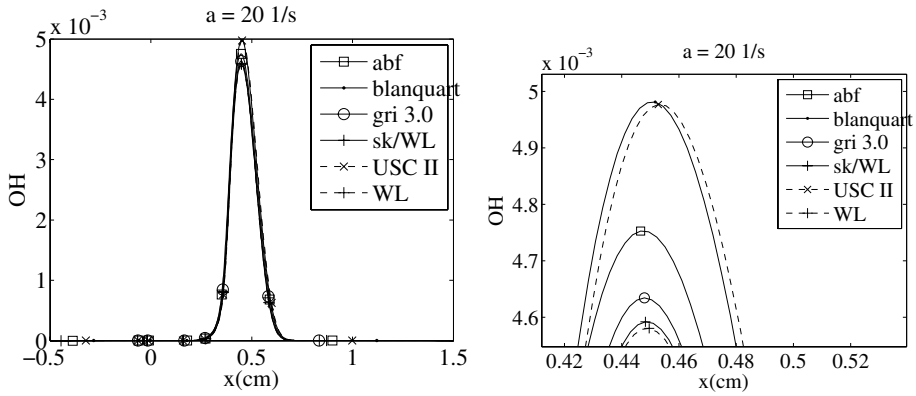

Fig. 18 OH mass fraction profile; zoom at the peak

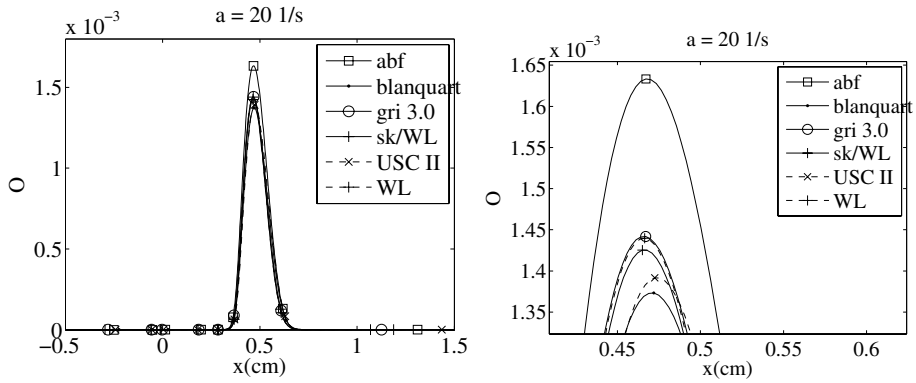

Fig. 19 O mass fraction profile; zoom at the peak

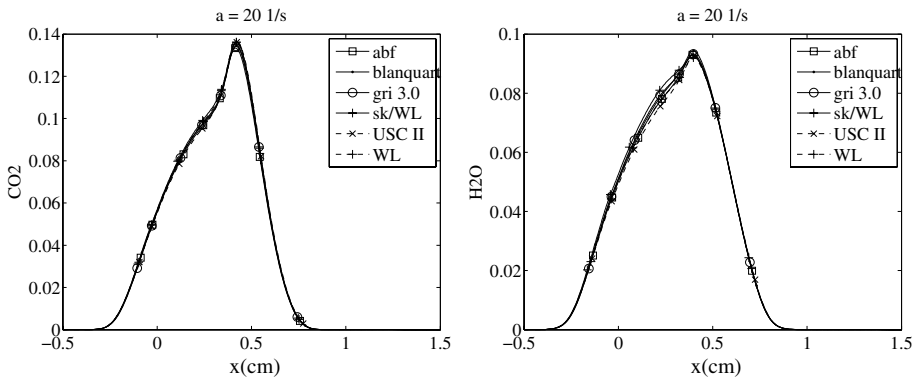

Fig. 20 CO_2 and H_2O mass fraction profiles

(no NOx reactions) are not shown here since it produced the same results as the original mechanism.

As can be seen from Figs. 15, 16, 17, 18 and 19, the selection of kinetic mechanism can have an influence in the flame characteristics, in the soot-related gas-phase species and therefore in soot prediction.

Figure 20 presents the two most important gas-phase species for radiative heat losses, CO_2 and H_2O mass fraction profiles, for all kinetic mechanisms used in this section.

The figure shows that the CO_2 and H_2O mass fraction profiles are slightly affected by the kinetic mechanisms.

Appendix 2: Soot model influence in soot predictions

In this section, a comparison between two sets of parameters for soot reactions within the same soot model is done for the 2D coflow flame. The first set of parameters is the one used in the present work, from [5], and the second is from [33]. Liu et al. [33] proposed a modified version of the two-equation model of Leung, with different sets of reaction rate constants and a special attention on the oxidation rates. This set was developed to fit the experiments of [38] for atmospheric non-smoking and smoking ethylene/air coflow diffusion flames. The comparison between both soot model parameters is presented in Table 4.

The comparison between the two sets of parameters is done for the exact same conditions presented in Sect. 3 for simulation a non-smoking ethylene coflow flame. The comparison is shown only for the soot volume integrated along the height of the burner in Fig. 21.

As shown in Fig. 21, the choice of the soot reactions parameters can have an important impact on the soot predictions. While the first set of parameters reaches the same peak

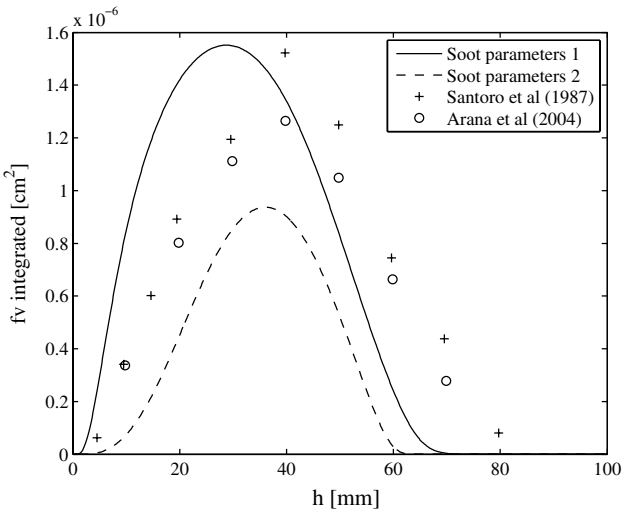

Fig. 21 f_v integrated comparison; symbols: experimental data [39] and [41]; solid line: present simulation with soot parameter 1—[5], parameter 2—[33]

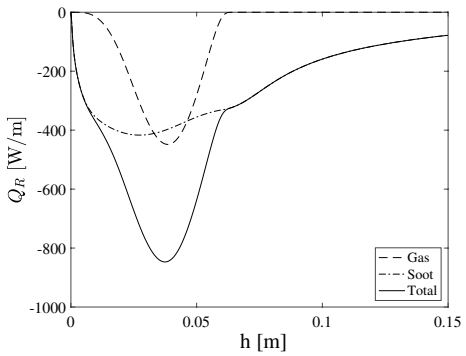

Fig. 22 Integrated radiation source term along the height for the each phase and the combined case with Soot Parameter 2—[33]

Table 4 Comparison of soot models; only the differences are shown

Reaction	Soot parameter 1 [5]	Soot parameter 2 [33]
Thermop. vel. const.	$C_i = 0.65$	$C_i = 0.67$
Nucleation	$k_1 = 1.0 \times 10^3 \exp(-16,103/T)$	$k_1 = 1.7 \exp(-7,548/T)$
Surf. Growth	$k_2 = 1.75 \times 10^3 \exp(-10,064/T)$	$k_2 = 6 \exp(-6,038/T)$
	$f(S) = \sqrt{S}$	$f(S) = S$
Oxid. by O_2	R_3	$R_3 f_{O_2}$
		$f_{O_2} = (1 + \exp[-(T - 1,650)/80])^{-1}$
Oxid. by OH	R_4	$R_4 f_{OH}$
		$f_{OH} = (1 + \exp[-(T - 1,675)/70])^{-1}, T \geq 1675$ K
		$f_{OH} = (1 + \exp[-(T - 1,675)/50])^{-1}, 1600K < T < 1675$ K
		$f_{OH} = 0.1824 \times (1 + \exp[-(T - 1,600)/85])^{-1}, T \leq 1600$ K
Oxid. by O	R_5	Not considered

of soot amount as the experiment, but at a lower height, the second set of parameter did neither reach the same amount of soot not the maximum soot prediction position, even though that set was fitted to do so in the original paper [33]. The maximum soot volume fraction was $f_{v,max} = 7.1$ ppm and $f_{v,max} = 5.3$ ppm, for Soot Parameters 1 and 2, respectively.

Similar to the analysis of radiative heat losses for model with Soot Parameter 1 (shown in Fig. 10), Fig. 22 presents the integrated radiation source term for soot model with Parameter 2.

Similar trend was found, the gas-phase radiation is the most important contribution, being responsible for 75% of the total radiative heat loss, while soot radiation is responsible for the remaining 25%. It is important to note that using Parameter 2, the amount of soot produced is less for the same flame; therefore, the soot radiation is less than with parameter 1. This results in higher overall temperature of the flame, with peak temperature of $T_{max} = 2103$ K, and higher gas-phase radiation.

References

1. Finlayson-Pitts BJ, Pitts JN (1997) Tropospheric air pollution: ozone, airborne toxics, polycyclic aromatic hydrocarbons, and particles. Science 276(5315):1045–1051. https://doi.org/10.1126/science.276.5315.1045
2. Bond TC, Doherty SJ, Fahey DW, Forster PM, Berntsen T, DeAngelo BJ, Flanner MG, Ghan S, Kärcher B, Koch D, Kinne S, Kondo Y, Quinn PK, Sarofim MC, Schultz MG, Schulz M, Venkataraman C, Zhang H, Zhang S, Bellouin N, Guttikunda SK, Hopke PK, Jacobson MZ, Kaiser JW, Klimont Z, Lohmann U, Schwarz JP, Shindell D, Storelvmo T, Warren SG, Zender CS (2013) Bounding the role of black carbon in the climate system: a scientific assessment. J Geophys Res: Atmos 118(11):5380–5552. https://doi.org/10.1002/jgrd.50171
3. Bourdrel T, Bind M-A, Béjot Y, Morel O, Argacha J-F (2017) Cardiovascular effects of air pollution. Arch Cardiovasc Dis 110(11):634–642. https://doi.org/10.1016/j.acvd.2017.05.003
4. WHO: World Health Organization (2018) Household air pollution and health [cited 3 Nov 2018]. http://www.who.int/en/news-room/fact-sheets/detail/household-air-pollution-and-health
5. Liu F, Guo H, Smallwood GJ, Gulder OL (2002) Effects of gas and soot radiation on soot formation in a coflow laminar ethylene diffusion flame. J Quant Spectrosc Radiat Transf 73(2–5):409–421
6. Liu F, Guo H, Smallwood GJ (2004) Effects of radiation model on the modeling of a laminar coflow methane/air diffusion flame. Combust Flame 138(1):136–154. https://doi.org/10.1016/j.combustflame.2004.04.007
7. Demarco R, Nmira F, Consalvi J (2013) Influence of thermal radiation on soot production in laminar axisymmetric diffusion flames. J Quant Spectrosc Radiat Transf 120:52–69. https://doi.org/10.1016/j.jqsrt.2013.02.004
8. Chu H, Consalvi J-L, Gu M, Liu F (2017) Calculations of radiative heat transfer in an axisymmetric jet diffusion flame at elevated pressures using different gas radiation models. J Quant Spectrosc Radiat Transf 197:12–25. https://doi.org/10.1016/j.jqsrt.2017.02.008**(The Eight International Symposium on Radiative Transfer)**
9. Xin Y, Liang W, Liu W, Lu T, Law CK (2015) A reduced multicomponent diffusion model. Combust Flame 162(1):68–74. https://doi.org/10.1016/j.combustflame.2014.07.019
10. Giovangigli V (2015) Multicomponent transport in laminar flames. Proc Combust Inst 35(1):625–637
11. Burali N, Lapointe S, Bobbitt B, Blanquart G, Xuan Y (2016) Assessment of the constant non-unity Lewis number assumption in chemically-reacting flows. Combust Theor Model 20(4):632–657. https://doi.org/10.1080/13647830.2016.1164344
12. Williams FA (1985) Combustion theory (Combustion Science and Engineering Series). The Benjamin/Cummings Publishing Company, Inc., San Francisco
13. Poinsot T, Veynante D (2005) Theoretical and numerical combustion. RT Edwards Incorporated, New York
14. Law CK (2006) Combustion physics. Cambridge University Press, Cambridge
15. Bongers H, Goey LPHD (2003) The effect of simplified transport modeling on the burning velocity of laminar premixed flames. Combust Sci Technol 175(10):1915–1928. https://doi.org/10.1080/713713111
16. Cuenot B, Poinsot T (1996) Asymptotic and numerical study of diffusion flames with variable Lewis number and finite rate chemistry. Combust Flame 104(1–2):111–137
17. Ju Y, Guo H, Liu F, Maruta K (1999) Effects of the Lewis number and radiative heat loss on the bifurcation and extinction of CH_4/O_2–N_2–He flames. J Fluid Mech 379:165–190. https://doi.org/10.1017/S0022112098003231
18. Pitsch H, Riesmeier E, Peters N (2000) Unsteady flamelet modeling of soot formation in turbulent diffusion flames. Combust Sci Technol 158(1):389–406. https://doi.org/10.1080/00102200008947342
19. Dietzsch F, Scholtissek A, Hunger F, Hasse C (2018) The impact of thermal diffusion on the structure of non-premixed flames. Combust Flame 194:352–362. https://doi.org/10.1016/j.combustflame.2018.05.018
20. Turns SR (2000) An introduction to combustion. McGraw-Hill, New York
21. Zimmer L (2016) Numerical study of soot formation in laminar ethylene diffusion flames, Ph.D. thesis, Universidade Federal do Rio Grande do Sul. http://hdl.handle.net/10183/150754. Accessed 20 May 2020
22. Zimmer L, Pereira FM, van Oijen JA, de Goey LPH (2017) Investigation of mass and energy coupling between soot particles and gas species in modelling ethylene counterflow diffusion flames. Combust Theor Model 21(2):358–379. https://doi.org/10.1080/13647830.2016.1238512
23. Kennedy IM, Kollmann W, Chen J-Y (1990) A model for soot formation in a laminar diffusion flame. Combust Flame 81(1):73–85
24. Hoerlle CA, Pereira FM (2019) Effects of CO_2 addition on soot formation of ethylene non-premixed flames under oxygen enriched atmospheres. Combust Flame 203:407–423. https://doi.org/10.1016/j.combustflame.2019.02.016
25. Hoerlle CA, França FHR, Pagot PR, Pereira FM (2020) Effects of radiation modeling on non-premixed sooting flames simulations under oxyfuel conditions. Combust Flame 217:294–305. https://doi.org/10.1016/j.combustflame.2020.04.012 **(ISSN 0010-2180)**
26. Dworkin S, Smooke M, Giovangigli V (2009) The impact of detailed multicomponent transport and thermal diffusion effects on soot formation in ethylene/air flames. Proc Combust Inst 32(1):1165–1172. https://doi.org/10.1016/j.proci.2008.05.061
27. Barlow R, Karpetis A, Frank J, Chen J-Y (2001) Scalar profiles and NO formation in laminar opposed-flow partially premixed methane/air flames. Combust Flame 127(3):2102–2118
28. Smooke M, McEnally C, Pfefferle L, Hall R, Colket M (1999) Computational and experimental study of soot formation in a

coflow, laminar diffusion flame. Combust Flame 117(1–2):117–139. https://doi.org/10.1016/S0010-2180(98)00096-0
29. Carbonell D, Oliva A, Perez-Segarra C (2009) Implementation of two-equation soot flamelet models for laminar diffusion flames. Combust Flame 156(3):621–632. https://doi.org/10.1016/j.combustflame.2008.12.003
30. Domenico MD, Gerlinger P, Aigner M (2010) Development and validation of a new soot formation model for gas turbine combustor simulations. Combust Flame 157(2):246–258. https://doi.org/10.1016/j.combustflame.2009.10.015
31. Chen J, Liu Y, Rogg B (1993) CO–H_2–N_2/air diffusion flames: thermal radiation and transient effects. In: Peters N, Rogg B (eds) Reduced kinetic mechanisms for applications in combustion systems, vol 15. Springer, Berlin, pp 196–223
32. TNF (2016) International workshop on measurement and computation of turbulent nonpremixed flames (tnf): radiation models [cited 25 May 2015]. http://www.sandia.gov/TNF/radiation.html
33. Liu F, Guo H, Smallwood GJ, Gülder ÖL (2003) Numerical modelling of soot formation and oxidation in laminar coflow nonsmoking and smoking ethylene diffusion flames. Combust Theor Model 7(2):301–315
34. Wilke C (1950) A viscosity equation for gas mixtures. J Chem Phys 18(4):517–519
35. Mason EA, Saxena SC (1958) Approximate formula for the thermal conductivity of gas mixtures. Phys Fluids 1(5):361–369. https://doi.org/10.1063/1.1724352
36. Hirschfelder JO, Curtiss CF, Bird RB et al (1954) Molecular theory of gases and liquids, vol 26. Wiley, New York
37. Smooke M, Giovangigli V (1991) Formulation of the premixed and nonpremixed test problems. Lect Notes Phys 384:1–28. https://doi.org/10.1007/BFb0035363
38. Santoro R, Semerjian H, Dobbins R (1983) Soot particle measurements in diffusion flames. Combust Flame 51:203–218. https://doi.org/10.1016/0010-2180(83)90099-8
39. Santoro RJ, Yeh TT, Horvath JJ, Semerjian HG (1987) The transport and growth of soot particles in laminar diffusion flames. Combust Sci Technol 53(2–3):89–115. https://doi.org/10.1080/00102208708947022
40. Kennedy IM, Yam C, Rapp DC, Santoro RJ (1996) Modeling and measurements of soot and species in a laminar diffusion flame. Combust Flame 107(4):368–382. https://doi.org/10.1016/S0010-2180(96)00092-2
41. Arana CP, Pontoni M, Sen S, Puri IK (2004) Field measurements of soot volume fractions in laminar partially premixed coflow ethylene/air flames. Combust Flame 138(4):362–372. https://doi.org/10.1016/j.combustflame.2004.04.013
42. Iyer SS, Litzinger TA, Lee S-Y, Santoro RJ (2007) Determination of soot scattering coefficient from extinction and three-angle scattering in a laminar diffusion flame. Combust Flame 149(1–2):206–216. https://doi.org/10.1016/j.combustflame.2006.11.009
43. Zhang Q, Guo H, Liu F, Smallwood G, Thomson M (2009) Modeling of soot aggregate formation and size distribution in a laminar ethylene/air coflow diffusion flame with detailed PAH chemistry and an advanced sectional aerosol dynamics model. Proc Combust Inst 32(1):761–768. https://doi.org/10.1016/j.proci.2008.06.109
44. Dworkin SB, Zhang Q, Thomson MJ, Slavinskaya NA, Riedel U (2011) Application of an enhanced PAH growth model to soot formation in a laminar coflow ethylene/air diffusion flame. Combust Flame 158(9):1682–1695. https://doi.org/10.1016/j.combustflame.2011.01.013
45. Eaves NA, Thomson MJ, Dworkin SB (2013) The effect of conjugate heat transfer on soot formation modeling at elevated pressures. Combust Sci Technol 185(12):1799–1819. https://doi.org/10.1080/00102202.2013.839554
46. Eaves N, Dworkin S, Thomson M (2015) The importance of reversibility in modeling soot nucleation and condensation processes. Proc Combust Inst 35(2):1787–1794. https://doi.org/10.1016/j.proci.2014.05.036
47. Khosousi A, Dworkin SB (2015) Detailed modelling of soot oxidation by O2 and OH in laminar diffusion flames. Proc Combust Inst 35(2):1903–1910. https://doi.org/10.1016/j.proci.2014.05.152
48. ISF (2016) International sooting flame (ISF) workshop. http://www.adelaide.edu.au/cet/isfworkshop/data-sets/laminar/. Accessed 20 May 2020
49. Guo H, Liu F, Smallwood G, Gulder OL (2002) The flame preheating effect on numerical modelling of soot formation in a two-dimensional laminar ethylene-air diffusion flame. Combust Theor Model 6(2):173–187
50. Charest MRJ (2011) Numerical modelling of sooting laminar diffusion flames at elevated pressures and microgravity. Ph.D. thesis, University of Toronto
51. Ansys® Fluent (2015) Release 16.1, help system, Theory Guide, ANSYS, Inc
52. Smith G, Frenklach DGM, Moriarty N, Eiteneer B, Goldenberg M, Bowman C, Hanson R, Song S, Gardiner W, Lissianski V, Qin Z (2000) Gri-mech 3.0. http://combustion.berkeley.edu/gri-mech/. Accessed 20 May 2020
53. Appel J, Bockhorn H, Frenklach M (2000) Kinetic modeling of soot formation with detailed chemistry and physics: laminar premixed flames of C2 hydrocarbons. Combust Flame 121(1–2):122–136. https://doi.org/10.1016/S0010-2180(99)00135-2
54. Blanquart G, Pepiot-Desjardins P, Pitsch H (2009) Chemical mechanism for high temperature combustion of engine relevant fuels with emphasis on soot precursors. Combust Flame 156(3):588–607
55. Wang H, You X, Joshi AV, Davis SG, Laskin A, Egolfopoulos F, Law CK (2007) USC Mech Version II. High-temperature combustion reaction model of H2/CO/C1–C4 compounds
56. Wang H, Laskin A (1999) A comprehensive kinetic model of ethylene and acetylene oxidation at high temperatures. http://ignis.usc.edu/Mechanisms/C2-C4/c2.html. Accessed 20 May 2020
57. Luo Z, Yoo CS, Richardson ES, Chen JH, Law CK, Lu T (2012) Chemical explosive mode analysis for a turbulent lifted ethylene jet flame in highly-heated coflow. Combust Flame 159(1):265–274. https://doi.org/10.1016/j.combustflame.2011.05.023

Publisher's Note Springer Nature remains neutral with regard to jurisdictional claims in published maps and institutional affiliations.